Effects of metal-based additives on dehydrogenation process of 2NaBH 4 - MgH 2 system

Article *in* International Journal of Hydrogen Energy September 2022

DOI: 10.1016/j.ijhydene.2022.08.293

17 authors, including:

Yuanyuan Shang
Helmholtz-Zentrum Hereon

Julián Puszkiel
Helmut Schmidt University / University of the Federal Armed Forces Hamburg / H…

Palmarin Dansirima
Suranaree University of Technology

Dorothée Vinga Szabó
Karlsruhe Institute of Technology

Effects of metal-based additives on dehydrogenation process of $2NaBH_4 + MgH_2$ system

Yuanyuan Shang [a], Ou Jin [b,c], Julián Atillio Puszkiel [a,d], Fahim Karimi [a], Palmarin Dansirima [e], Chongsutthamani Sittiwet [e], Rapee Utke [e], Siriwat Soontaranon [f], Thi Thu Le [a], Gökhan Gizer [a], Dorothée Vinga Szabó [b,c,g], Stefan Wagner [b], Christian Kübel [b,g,h], Thomas Klassen [a,c], Martin Dornheim [a], Astrid Pundt [b,c], Claudio Pistidda [a,*]

[a] Department of Materials Design, Institute of Hydrogen Technology, Helmholtz Zentrum hereon GmbH, 21502, Geesthacht, Germany
[b] Institute for Applied Materials, Karlsruhe Institute of Technology, 76131, Karlsruhe, Germany
[c] Institute of Nanotechnology, Karlsruhe Institute of Technology, 76344 Eggenstein Leopoldshafen, Germany
[d] Helmut Schmidt University, Holstenhofweg 85, 22043, Hamburg, Germany
[e] School of Chemistry, Institute of Science, Suranaree University of Technology, Nakhon Ratchasima 3000, Thailand
[f] Synchrotron Light Research Institute, Nakhon Ratchasima 30000, Thailand
[g] Karlsruhe Nano Micro Facility, Karlsruhe Institute of Technology, 76344 Eggenstein Leopoldshafen, Germany
[h] Joint Research Laboratory Nanomaterials, Technical University of Darmstadt, Darmstadt 64206, Germany

HIGHLIGHTS

- Ti and Al based additives strongly enhances the material dehydrogenation properties.
- The formed Ti and Al borides stronghly influence the microstructural features of MgB_2.
- Crystallographic chemical theory of nucleation and growth is a potential tool to identify new additives.

Keywords:
Hydrogen storage
Borohydrides
Nucleation and growth
Kinetic modeling

ABSTRACT

We report a systematic investigation of the effect that selected metal based additives have on the dehydrogenation properties of the reactive hydride composite (RHC) model system $2NaBH_4+MgH_2$. Compared to the pristine system, the material doped with $3TiCl_3 \cdot AlCl_3$ exhibits superior dehydrogenation kinetics. The addition of $3TiCl_3 \cdot AlCl_3$ alters the controlling mechanism of the second dehydrogenation step making it change from a two dimensional interface controlled process to a two dimensional nucleation and growth controlled process. The microstructural investigation of the dehydrogenated $2NaBH_4+MgH_2$ *via* high resolution transmission electron microscopy (HRTEM) shows significant differences in the MgB_2 morphology formed in the doped and undoped systems. The MgB_2 has a needle like structure in the sample doped with $3TiCl_3 \cdot AlCl_3$, which is different from the plate like MgB_2 structure in the undoped sample. Moreover, nanostructured metal

* *Corresponding author*. Max Planck Straße 1, 21502 Geesthacht.
E mail address: claudio.pistidda@hereon.de (C. Pistidda).

based phases, such as TiB_2/AlB_2 particles, acting as heterogeneous nucleation sites for MgB_2 are also identified for the sample doped with $3TiCl_3 \cdot AlCl_3$.

Introduction

In recent years, the possibility of replacing non sustainable fossil fuel energy sources with renewable energy sources has been largely debated. In this scenario, hydrogen is considered as a potential energy vector capable of supporting this epochal transition [1–4]. Hydrogen has the highest energy density per mass, *i.e.*, almost 2.5 times of the energy density per mass of conventional fossil fuels such as methane, propane, and gasoline. As an example, under ambient conditions, the mass energy density of hydrogen is ~120 MJ kg ^{1}, while the values for methane, gasoline, and diesel are about 55.6, 46.4, and 45.6 MJ kg ^{1}, respectively [5]. However, hydrogen being the lightest element on the periodic table, its energy density per volume (0.003 kWh·L ^{1}) [6] is lower than the volumetric energy densities of methane, propane, and gasoline (4.2, 7.1, and 9.0 kWh·L ^{1}, respectively [7,8]). To overcome the volumetric energy density handicap, hydrogen is commonly compressed to pressures up to 700 bar or liquefied at cryogenic temperatures (*i.e.*, 253 °C), through energy demanding processes. For instance, the theoretical energy values spent for the isothermal compression of hydrogen up to 350 and 700 bar are 12% and 15% of its lower heating value (LHV), respectively, while 30% of its LHV is necessary for liquefaction [9]. An alternative method is to store hydrogen in metal based compounds chemically. This approach allows storing hydrogen in a solid state under low working pressure conditions, achieving at the same time high volumetric energy densities and high safety standards [10–19].

The possibility of reversibly storing hydrogen in metal hydrides was investigated in the early 1960s [20]. At that time, the use of complex metal hydrides such as $NaBH_4$, $LiBH_4$, *etc.* to store hydrogen was limited by the apparent irreversibility of their thermal decomposition products [21]. In fact, despite their appealing gravimetric and volumetric hydrogen capacity, complex metal hydrides are reversible only at extreme temperature and hydrogen pressure conditions. For instance, $LiBH_4$ could be partially rehydrogenated at 600 °C under 350 bar of hydrogen pressure [22]. For this reason, until the end of the 1990s, they mainly were investigated as one pass storage systems. The one pass storage method releases hydrogen upon water hydrolysis [21,23] in the presence of transition metal based catalysts. In 1996 the pioneering work of Bogdanovic and Schwickardi [24] opened the doors to the use of complex metal hydrides as reversible hydrogen storage systems. Since then, many efforts have been made to investigate the properties of this class of hydrides and to optimize their performance by using suitable catalysts and destabilizing agents [25,26].

As the result of this investigation effort, the reactive hydride composites (RHCs) approach was discovered. In this approach, two or more hydride species are combined to obtain a system with a still high hydrogen storage capacity but lower reaction enthalpy and high reversibility [27–29]. One of the RHCs that has been considered as a model system is $2NaBH_4 + MgH_2$ [30,31], owing to its significantly large gravimetric hydrogen storage capacity (7.8 wt%), stability in air (higher than RHCs containing $LiBH_4$, $Ca(BH_4)_2$, $LiNH_2$, $Mg(NH_2)_2$, *etc.*) and low cost of the raw materials, *i.e.* 10 times cheaper than the Li containing system [32].

In this system, the dehydrogenation is expected to occur following a two step reaction [30]:

$$2NaBH_4 + MgH_2 \leftrightarrows 2NaBH_4 + Mg + H_2 \quad (1)$$

$$2NaBH_4 + Mg \leftrightarrows 2NaH + MgB_2 + 4H_2 \quad (2)$$

However, depending on the temperature and hydrogen pressure used, reaction intermediates such as the eutectic molten phase of $NaH/NaBH_4$ [33], $NaMgH_3$ [31], and products such as Na, $NaB_{12}H_{12}$, and B can be formed [30,34]. Owing to a theoretical dehydrogenation enthalpy (for the reaction that from $2NaBH_4 + MgH_2$ lead to $2NaH + MgB_2 + 4H_2$) of 62 kJ mol ^{1} H_2 and an entropy of 26.2 kJ mol ^{1} the expected dehydrogenation temperature at 1 bar H_2 is ca. 350 °C that is considerably lower than the dehydrogenation temperature of pure $NaBH_4$ (ca. 500 °C) [35,36]. These properties make the $2NaBH_4 + MgH_2$ system a potential candidate for medium temperature hydrogen storage applications and heat storage applications. However, despite the improved thermodynamic properties, the formation of $NaH + MgB_2$ although starts at about 350 °C [31], proceeds speedily only at temperature as high as 450 °C.

In the attempt to find appropriate catalysts to improve the hydrogen storage properties of RHCs, the use of transition metal (TM) based additives such as TiF_4, $ZrCl_4$, and Sc_2O_3 proved to be a suitable approach [37–42]. In many cases, by adding small amounts of TM based additives, the reaction kinetics can be accelerated by a factor of ten [42]. For instance, Bosenberg et al. [42] found that by adding Sc_2O_3 and $ZrCl_4$ to $2LiBH_4 + MgH_2$, the incubation stage for the dehydrogenation of $LiBH_4$ vanishes, thus the dehydrogenation reaction time is significantly shortened, *e.g.*, from 25 h to 5 h. Karimi et al. [43] found that by using the NbF_5 additive, the dehydrogenation temperature of the $Ca(BH_4)_2 + MgH_2$ was decreased from 350 °C to 250 °C. Bonatto Minella et al. [38] showed that by adding 5 mol% of TiF_4 into the $Ca(BH_4)_2 + MgH_2$ system, the formation of transition metal boride nanoparticles can be observed, and the onset dehydrogenation temperature decreases from 350 °C to 125 °C. In these works, the added TM based additives react with the starting materials to form more stable compounds such as ZrB_2 and TiB_2, with an average particle size between 5 and 20 nm. The crystallographic structure and the interface location of those TM based compounds appear to affect the nucleation and growth of new

phases, *e.g.*, MgB_2 in the RHCs. Bosenberg et al. [42] proposed that the better nucleation behavior of MgB_2 can be ascribed to the microstructural similarities between the newly generated TM based phases and the nucleating MgB_2, according to nucleation and growth knowledge accessible from metallurgical areas, *i.e.*, edge to edge matching model [44], which was recently further substantiated by Jin et al. [45]. For heterogeneous nucleation substrates, the coherent energy of the interface between the parental phase and the new phase is minimized by lowering the lattice mismatch at the interface. For example, Jin et al. [45] reported the elastic strain energy density along <10 10>TiB_2/AlB_2 || <10 10>MgB_2 is more than 6 times smaller than that induced at the interface between Mg and MgB_2 along <10 10>Mg || <10 10>MgB_2. Therefore, the strain energy between the parental phase (TiB_2/AlB_2) and the new phase (MgB_2) can be minimized, and these phases can act as the active nucleation sites for MgB_2 to enhance the kinetics for the second dehydrogenation step. Nevertheless, it is not clear if the proposed TM based additives' mechanism of work also applies to all the RHC systems.

Taking $2NaBH_4 + MgH_2$ as a model system, the present work aims to investigate further the role of the microstructural properties of the additive/additive derived phases on the nucleation of MgB_2. The selected additives were chosen based on previously published works. The halogen containing additives were chosen based on the possibility of altering the material's thermodynamic stability by anion substitution [46], and based on the capability of forming boride nanoparticles that can influence the material reaction kinetics [30,32,47,48]. Instead, $Mg(OH)_2$ was added due to the possibility to form upon milling well dispersed MgO particles, which can improve MgH_2's dehydrogenation properties [49]. Volumetric technique, X ray diffraction (XRD), Fourier transform infrared spectroscopy (FTIR), equilibrium composition calculation, transmission electron microscopy (TEM), and small angle X ray scattering (SAXS) methods were used to investigate the material properties, with the results reported in the following.

Experimental

Commercially available powders of $NaBH_4$ (≥98.0% purity, Sigma Aldrich), MgH_2 (95% purity, Rockwood Lithium GmbH), MgF_2 (99.99% purity, Umicore Materials AG), $3TiCl_3 \cdot AlCl_3$ (~76–78% $TiCl_3$ purity, Fisher Scientific), VCl_3 (99% purity, Alfa Aesar), and $Mg(OH)_2$ (95–100.5% purity, Alfa Aesar) were used as starting materials. The specimens investigated in this work were prepared by milling 3 g of $2NaBH_4 + MgH_2$ with and without 5 mol% of additives (*i.e.*, MgF_2, $3TiCl_3 \cdot AlCl_3$, VCl_3, and $Mg(OH)_2$) in a Spex 8000 M Mixer Mill for 400 min, as shown in Table 1. Stainless steel vial and balls with a diameter of 10 mm were used to perform the milling, with a ball to powder ratio of 20:1. The material handling and milling were performed under a continuously purified Ar atmosphere, with H_2O and O_2 levels lower than 1 ppm.

The dehydrogenation experiments were carried out using an in house made Sievert's apparatus. For each analysis, about 170 mg of material were desorbed under 0.15 bar of hydrogen pressure, increasing the temperature from room conditions to 450 °C with a heating rate of 3 °C/min, and then keeping the material under isothermal conditions at 450 °C for 5–8 h.

The crystalline phase identification was carried out by *ex situ* powder XRD method using a Bruker D8 Discover diffractometer using Cu Kα (λ 1.54184 Å) radiation operated at 1000 mA and 50 kV. The measured 2θ range is 10°–90° with steps of 10°, for each step, the exposure time is 400 s. To protect the sample from air and moisture, a polymethyl methacrylate (PMMA) airtight sample holder from Bruker was used during the measurements. The average crystallite size was obtained by the full width at half maximum (FWHM) of the diffraction peaks *via* Scherrer formula [50]:

$$t \quad \frac{0.9\lambda}{\beta \cos \theta} \tag{3}$$

where t is the crystallite size, 0.9 is the particle shape factor, λ is the X ray wavelength, β is the FWHM, and θ is the Bragg angle.

Fourier transform infrared spectroscopy (FT IR) technique was applied to characterize the corresponding phases of the as milled samples, using an Agilent Technologies Cary 620 FT IR located inside an Ar filled glovebox (O_2 and H_2O levels lower than 1 ppm). Each spectrum was recorded in the range of 650 cm^{-1} to 4000 cm^{-1} with a resolution of 4 cm^{-1}.

Small angle X ray scattering (SAXS) measurements were carried out at Beamline 1.3W: SAXS/WAXS, Synchrotron Light Research Institute (SLRI), Thailand. This beamline offers X ray energy of 9 keV, with a sample to detector distance (SSD) of 4297 mm (calibrated using SEBS block co polymer standard sample). The accessible q range was between 0.05 and 1.5 nm^{-1}, and the exposure time was chosen to be 60 s. The beam size at the sample position was 1×1 mm^2 and a Rayonix SX165 CCD detector was implemented. The SAXS pattern of the samples and the backgrounds were recorded. These patterns were normalized by the beam intensity and its X ray transmission. Then, the 1D SAXS profiles were obtained by radial averaging the resultant background subtracted pattern. Data pre processing was done *via* software of SAXSIT version 4.48 (Small Angle X ray Scattering Image Tool, in house developed software at SLRI).

Table 1 – Prepared $2NaBH_4$+MgH_2 RHCs doped with additives.

No.	Composition	Designation
1	$2NaBH_4 + MgH_2$	Na RHC
2	$2NaBH_4 + MgH_2$ + 5mol% MgF_2	Na RHC + 5 mol% MgF_2
3	$2NaBH_4 + MgH_2$ + 5mol% $3TiCl_3$ $AlCl_3$	Na RHC + 5 mol% $3TiCl_3$ $AlCl_3$
4	$2NaBH_4 + MgH_2$ + 5mol% VCl_3	Na RHC + 5 mol% VCl_3
5	$2NaBH_4 + MgH_2$ + 5mol% $Mg(OH)_2$	Na RHC + 5 mol% $Mg(OH)_2$

Equilibrium composition calculations were carried out with the HSC Chemistry software 9.7.2[51]. Pure materials were taken into account for the calculations. The conditions for the calculations were as follows: dehydrogenation from room temperature (RT) to 500 °C under 1 bar of H_2 pressure. The most favorable reactions were identified by combining Gibbs minimization equilibrium with selected solid and gas species. The obtained results represent ideal phase equilibrium com positions useful to predict the possible reaction. The com pound $NaMgH_3$ was added to the database. The enthalpy, entropy, and heat capacity of the $NaMgH_3$ were obtained from Refs. [52–54]. All the calculations can be seen in the Sup porting information (Figs. S2–11 and Tables S2–11).

For the TEM investigations, the sample powder was dispersed in toluene and ultra sonicated for 1 min at room temperature and subsequently dropped onto Lacey carbon coated TEM copper grids. To avoid oxidation of the mate rials, these operations were carried out under argon atmo sphere in the glovebox. The prepared sample was then introduced into the TEM column using a vacuum transfer holder 648 (Gatan Inc., USA). TEM experiments were per formed on a Themis Z 60–300 (Thermo Fisher Scientific Inc., USA) equipped with a monochromator and double aberration correctors (probe and image Cs correctors), operated at 300 kV. Scanning TEM (STEM) images and Energy dispersive X ray spectroscopy (EDX) elemental mapping were acquired *via* a high angle annular dark field (HAADF) detector with a convergence angle of 21.5 mrad and a camera length of 93 mm. Selected area electron diffraction (SAED) patterns and high resolution TEM (HRTEM) images were recorded using an OneView camera (Gatan Inc., USA).

Kinetic modeling was done by using the Sharp and Jones method [55,56], in which the experimental data can be expressed as follows:

$$F(\alpha) \quad A(\frac{t}{t_{0.5}}) \tag{4}$$

where α is the reaction fraction, t is the reaction time, $t_{0.5}$ is the time at α 0.5, and A is the rate constant. $F(\alpha)$ was considered as the hydrogen storage capacity over the maximum capacity for the second dehydrogenation process of each sample. The portion of the dehydrogenation curve used here is 0.1–0.7 (for pure Na RHC) and 0.1–0.8 (for Na RHC + 5 mol% $3TiCl_3 \cdot AlCl_3$) of the overall hydrogen storage capacity for the second step. Firstly, the kinetic curves of the second step for each sample were normalized from 0 to 1, as shown in Fig. S13. Subse quently, different fitting models were used to fit the second dehydrogenation step, as shown in Table S12. The criterion for deciding whether a model is feasible is as follows: the slope of the fitted curve should be close to 1, the intercept should be close to 0, and the fitting coefficient of determination (R^2) should be close to 1.

Results and discussion

Structural characterization of the as-milled materials

The diffraction patterns acquired for the as milled materials are reported in Fig. 1(a). The diffraction peaks that dominate the patterns of $2NaBH_4 + MgH_2$ (Na RHC), Na RHC + 5 mol% $3TiCl_3 \cdot AlCl_3$, and Na RHC + 5 mol% VCl_3 are those of $NaBH_4$ and MgH_2 and in the case of Na RHC + 5 mol% MgF_2 and Na RHC + 5 mol% $Mg(OH)_2$, the diffraction peaks of Mg are also detectable. The presence of the Mg peaks is expected as it is the main impurity of the purchased MgH_2 (purity is 95%). Interestingly, for all the investigated materials, no diffraction signals related to the additives' presence or the products of their interaction with $NaBH_4$ and MgH_2 are visible. This can be attributed to the small amount of these compounds or because such compounds are nanostructured after ball mill ing. Investigations on the possible chemical alteration of the bending and stretching modes of the B–H bonds due to the presence of halogen and oxidize containing additives were performed. Thus, the as milled samples were characterized *via* FT IR. The obtained FTIR spectra are presented in Fig. 1(b). The features of the $[BH4]^-$ group can be observed in all the spectra, *e.g.*, the B–H bending vibration (~1110 cm ^{1}) and the B–H stretching vibrations (2000 2520 cm ^{1}), which is in good agreement with the spectral data from the literature [57,58].

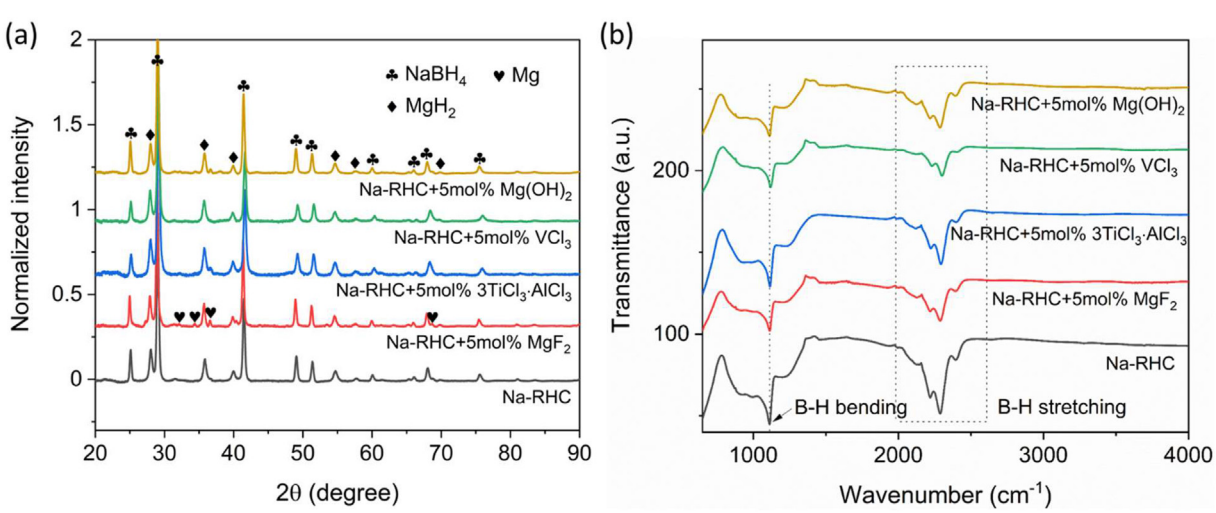

Fig. 1 – (a) XRD and (b) FTIR results of as milled Na-RHC + 5 mol% MgF_2, $3TiCl_3 \cdot AlCl_3$, VCl_3, and $Mg(OH)_2$ samples.

These results show that the B–H bonds in the $[BH_4]^-$ groups are unaltered by the addition of the additives and that no H to Cl or H to F substitution took place. For what it concerns, the sample containing $Mg(OH)_2$ although we do not possess direct proof likely reacted with $NaBH_4$ to form NaOH, B, and H_2. Considering that the unit cell dimension of $NaBH_4$ as well as the FTIR signals of $NaBH_4$ (see Table S1) in the investigated systems appear to be unaffected by the presence of the dop ants, we can assume that under the investigated conditions no anionic substitution occurs between the H of $NaBH_4$ and the halogen species contained in the additives.

Dehydrogenation investigations

The hydrogen desorption curves of all the Na RHC samples are shown in Fig. 2(a). The kinetic curves for the starting materials of $NaBH_4$ and MgH_2 were plotted for compasison. As shown in Eqs. (1) and (2), the dehydrogenation process of the Na RHC consists of two steps. The first step refers to the dehydrogenation of MgH_2, and the second step corresponds to the dehydrogenation of $NaBH_4$ and the formation of the solid phases NaH and MgB_2. The pure Na RHC can release 7.5 wt% of H_2 in 8 h. The sample doped with MgF_2 shows the largest hydrogen release of 8.7 wt%, while the total hydrogen storage capacity of the material containing $3TiCl_3{\cdot}AlCl_3$ is 8.0 wt%. The sample doped with $Mg(OH)_2$ appears to possess the same hydrogen capacity as the pure Na RHC, *i.e.*, 7.5 wt%. The sample doped with VCl_3 has a hydrogen capacity of about 6.7 wt%. As shown in Fig. 2(a), all additives shortened the in cubation time for the first step of dehydrogenation (about 2.1 wt% of hydrogen is released). Based on the data reported in Fig. 2(a), the magnitude of this effect appears in the following order: $3TiCl_3{\cdot}AlCl_3 > VCl_3 > MgF_2 > Mg(OH)_2$. Also, when it comes to the second step, the sample doped with $3TiCl_3{\cdot}AlCl_3$ shows the fastest kinetics. The XRD patterns of the pure and MgF_2, $3TiCl_3{\cdot}AlCl_3$, VCl_3, and $Mg(OH)_2$ doped Na RHCs desorbed until the end of the first step in Fig. S1 confirm that the first dehydrogenation step is related only to the decomposition of MgH_2. Fig. 2(b) shows the XRD patterns ac quired for all the samples after dehydrogenation. Under the same dehydrogenation condition, the presented phases in pure $NaBH_4$ and MgH_2 are $NaBH_4$ and Mg, respectively. All the patterns of the Na RHC system show the characteristic peaks of Na/NaH and MgB_2. The peaks of NaCl or NaF can also be detected in the samples doped with halogen containing ad ditives. This finding supports our first claim that the halogen containing phases are nanostructured after milling. Note that for the pristine and $Mg(OH)_2$ doped samples, the diffraction peaks of $NaBH_4$ are still visible, suggesting that the dehydro genation reaction is not complete, which is in good agreement with the kinetic performances shown in Fig. 2(a). Moreover, based on these data we can safely state that the achievement of capacities higher than expected (*i.e.*, the samples doped with 5 mol% of MgF_2 and $3TiCl_3{\cdot}AlCl_3$ in Fig. 2(b)) results from the fact that under the applied hydrogen pressure and tem perature conditions NaH partially decomposed to Na. Although due to a partial unassisted decomposition of $NaBH_4$ the formation of amorphous or nanostructured B containing phases (e.g.boron and $B_{12}H_{12}$) is potentially possible, in the investigated systems can be excluded based on the previous research [59].

Equilibrium phase compositions

In order to understand the reaction mechanism of the dehy drogenation process of the Na RHCs with and without addi tives, the equilibrium phase composition calculations were performed by minimizing the Gibbs free energy *via* the HSC Chemistry software [51]. The calculated results are shown in Table 2. For the MgF_2, $3TiCl_3{\cdot}AlCl_3$, and VCl_3 doped samples, NaCl and NaF were calculated to be the potential products, which is in good agreement with the XRD results shown in

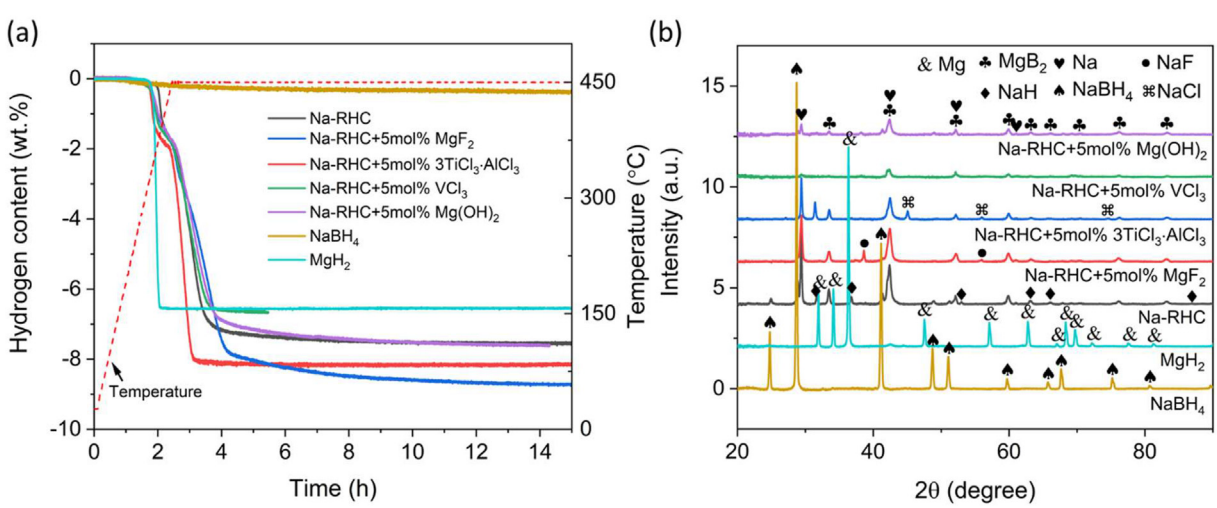

Fig. 2 – (a) Dehydrogenation curves and (b) corresponding XRD patterns after dehydrogenation of pure $NaBH_4$, MgH_2, Na-RHC, Na-RHC + 5 mol% MgF_2, $3TiCl_3{\cdot}AlCl_3$, VCl_3, and $Mg(OH)_2$ samples. The dehydrogenation measurements were performed under 15 kPa backpressure while heating from room temperature to 450 °C with a heating rate of 3 °C/min and then kept isothermal at 450 °C for 5–8 h. (For interpretation of the references to color/colour in this figure legend, the reader is referred to the Web version of this article.)

Table 2 – The calculated equilibrium phase compositions of Na-RHC + 5 mol% MgF_2, $3TiCl_3{\cdot}AlCl_3$, VCl_3, and $Mg(OH)_2$ after dehydrogenation. The calculations are based on the following conditions: from RT to 500 °C under 1 bar of H_2 pressure.

System	Dehydrogenation pathway
$1.8\ NaBH_{4(s)} + MgH_{2(s)}$	$1.8\ NaH_{(s)} + 0.1\ Mg_{(s)} + 0.90\ MgB_{2(s)} + 3.7H_{2(g)}$
$1.8\ NaBH_{4(s)} + MgH_{2(s)} + 0.015\ MgF_{2(s)}$	$1.77\ NaH_{(s)} + 0.115\ Mg_{(s)} + 0.03\ NaF_{(s)} + 0.90\ MgB_{2(s)} + 3.7150H_{2(g)}$
$1.865\ NaBH_{4(s)} + MgH_{2(S)} + 0.1125\ TiCl_{3(S)} + 0.0375\ AlCl_{3(S)}$	$1.415\ NaH_{(S)} + 0.0375\ Al_{(S)} + 0.18\ Mg_{(S)} + 0.45\ NaCl_{(S)} + 0.82\ MgB_{2(S)} + 0.1125\ TiB_{2(S)} + 4.0225H_{2(g)}$
$1.8\ NaBH_{4(s)} + MgH_{2(s)} + 0.015\ VCl_{3(s)}$	$1.755\ NaH_{(s)} + 0.115\ Mg_{(s)} + 0.045\ NaCl_{(s)} + 0.885\ MgB_{2(s)} + 0.015\ VB_{2(s)} + 3.7225H_{2(g)}$
$1.8\ NaBH_{4(s)} + MgH_{2(s)} + 0.015\ Mg(OH)_{2(s)}$	$1.8\ NaH_{(s)} + 0.085\ Mg_{(s)} + 0.03\ MgO_{(s)} + 0.90\ MgB_{2(s)} + 3.715H_{2(g)}$

Fig. 2(b). According to the minimization of Gibbs free energy, the formation of TiB_2 and VB_2 is also possible during the dehydrogenation process, which is well suited to the reported TM based borides characterized by TEM from literature [42,60–62]. These phases are not detected by XRD as shown in Fig. 2 (b). Hence, in the following section further structural characterizations are presented, revealing the presence of these species.

Microstructural and morphology properties

As previously mentioned, the addition of the TM based additives influences the kinetic behavior of $2NaBH_4$+MgH_2. Similar behaviors are generally observed also for the systems $2LiBH_4$+MgH_2 and $Ca(BH_4)_2$+MgH_2 doped with TM based additives [63]. However, for the system $2NaBH_4 + MgH_2$, only the additive $3TiCl_3{\cdot}AlCl_3$ appears to enhance the kinetic behavior of the second dehydrogenation step. The use of additives prior to grinding frequently results in noticeable microstructural alterations. This is related to the formation of hard nano particles, which during milling improve the grain refinement process and, as a result, reduce the diffusion length distances in the system and the enlarged reactant contact area. For this reason, the crystallite sizes of $NaBH_4$ and MgH_2 after milling and of MgB_2 after dehydrogenation were calculated for all investigated samples (Table 3) by using the Scherrer formula on the related XRD peaks. On the one hand, the crystallite sizes of the $NaBH_4$ and MgH_2 vary from one additive to the other. In the case of the sample containing MgF_2, the crystallite sizes of the $NaBH_4$ and MgH_2 are 30.2 ± 1.5 nm and 21.2 ± 1.1 nm, respectively. While for the sample containing $3TiCl_3{\cdot}AlCl_3$, crystallite sizes of the $NaBH_4$ and MgH_2 are 20.9 ± 1.0 nm and 15.7 ± 0.8 nm, respectively. On the other hand, the crystallite size values for MgB_2 in the desorbed materials are around 13 nm, thus independent of the presence of the additives.

As the reaction rate for the second step is related to the nucleation and growth of MgB_2 particles [42], the morphology of the formed MgB_2 is investigated *via* different TEM techniques. Owing to the fastest achieved dehydrogenation kinetics, the sample selected for this investigation is the dehydrogenated Na RHC doped with $3TiCl_3{\cdot}AlCl_3$. Pure Na RHC is used for comparison.

According to Fig. 3(a) and (b), the pure Na RHC contains plate shaped MgB_2. The plates are visible in bright contrast in Fig. 3(a). Higher magnification images suggest that these MgB_2 particles have most likely plate like morphology, as shown in the high angle annular dark field (HAADF) image in Fig. 3(c) and the related diffraction pattern Fig. 3(d). The diffraction pattern of $NaBH_4$ is not visible in Fig. 3(b) and (d) due to the fact that $NaBH_4$ readily decomposes under the electron beam while acquiring the diffraction images. The corresponding energy dispersive X ray spectroscopy (EDX) mappings of different elements containing Na, Mg, and Cu are shown in Fig. 3(e)–(h). The results confirm the plate like morphology of MgB_2, as revealed previously. Note that the existence of Cu originates from the use of the Cu grid for TEM measurements.

Differently, as shown in Fig. 4(a) and (b), the MgB_2 particles in the sample doped with 5 mol% $3TiCl_3{\cdot}AlCl_3$ are distributed more uniformly. The HAADF image in Fig. 4(c) illustrates a typical needle like structure of MgB_2, in the 2D image. However, the 3D morphology has not been identified yet. We stay with the designation "needle" here because of its appearance in the 2D images. The corresponding electron energy loss spectroscopy (EELS) mapping data in Fig. 4(d) confirms the presence of several elements, *e.g.*, Mg, B, and Ti, for the area in Fig. 4(c), and the MgB_2 particles are surrounded by Ti containing compounds. Except for MgB_2, the

Table 3 – Crystallite size of $NaBH_4$ and MgH_2 in the milled and MgB_2 in the dehydrogenated Na-RHC + 5 mol% MgF_2, $3TiCl_3{\cdot}AlCl_3$, VCl_3, and $Mg(OH)_2$ samples, as determined by using Scherrer formula on the related XRD peaks.

Composition	As milled		After dehydrogenation
	Crystallite size of $NaBH_4$ (nm)	Crystallite size of MgH_2 (nm)	Crystallite size of MgB_2 (nm)
Na RHC	25.0 ± 1.3	16.6 ± 0.8	13.9 ± 0.7
Na RHC + 5 mol% MgF_2	30.2 ± 1.5	21.2 ± 1.1	13.7 ± 0.7
Na RHC + 5 mol% $3TiCl_3$ $AlCl_3$	20.9 ± 1.0	15.7 ± 0.8	14.3 ± 0.7
Na RHC + 5 mol% VCl_3	22.7 ± 1.1	16.8 ± 0.8	12.9 ± 0.6
Na RHC + 5 mol% $Mg(OH)_2$	26.0 ± 1.3	18.9 ± 0.9	13.7 ± 0.7

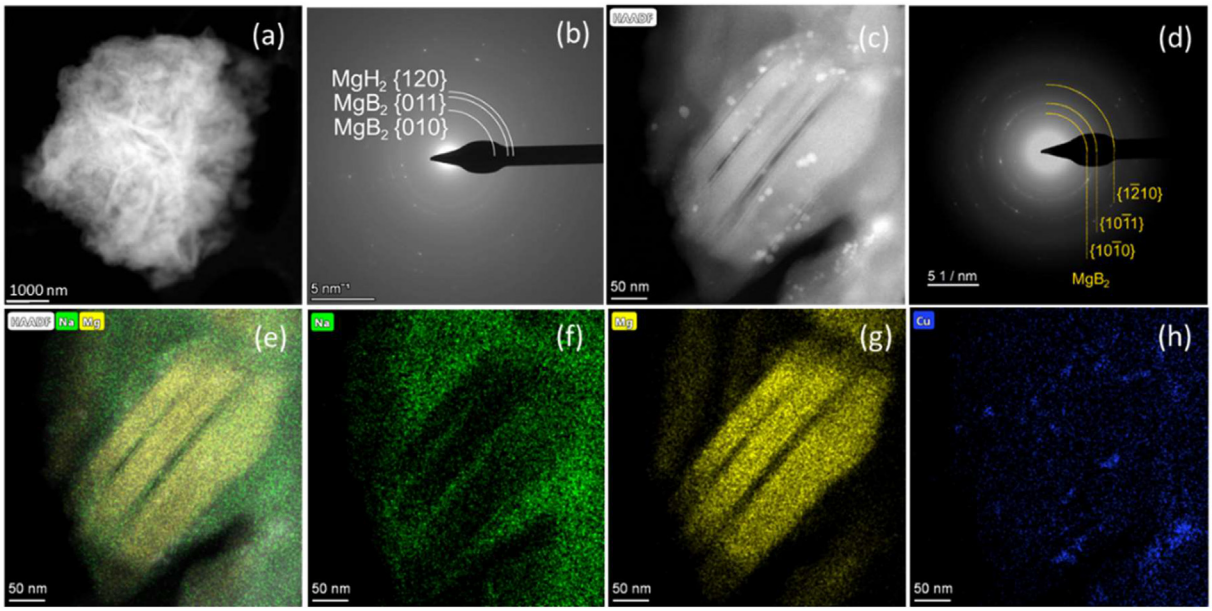

Fig. 3 – (a) TEM and (b) the corresponding FFT images of the pure Na-RHC sample after dehydrogenation. (c) TEM and (d) the corresponding FFT images at higher magnification. The corresponding EDX (e) overlap mapping of Na and Mg, (f) mapping of Na, (g) mapping of Mg, and (h) mapping of Cu for the area in (c).

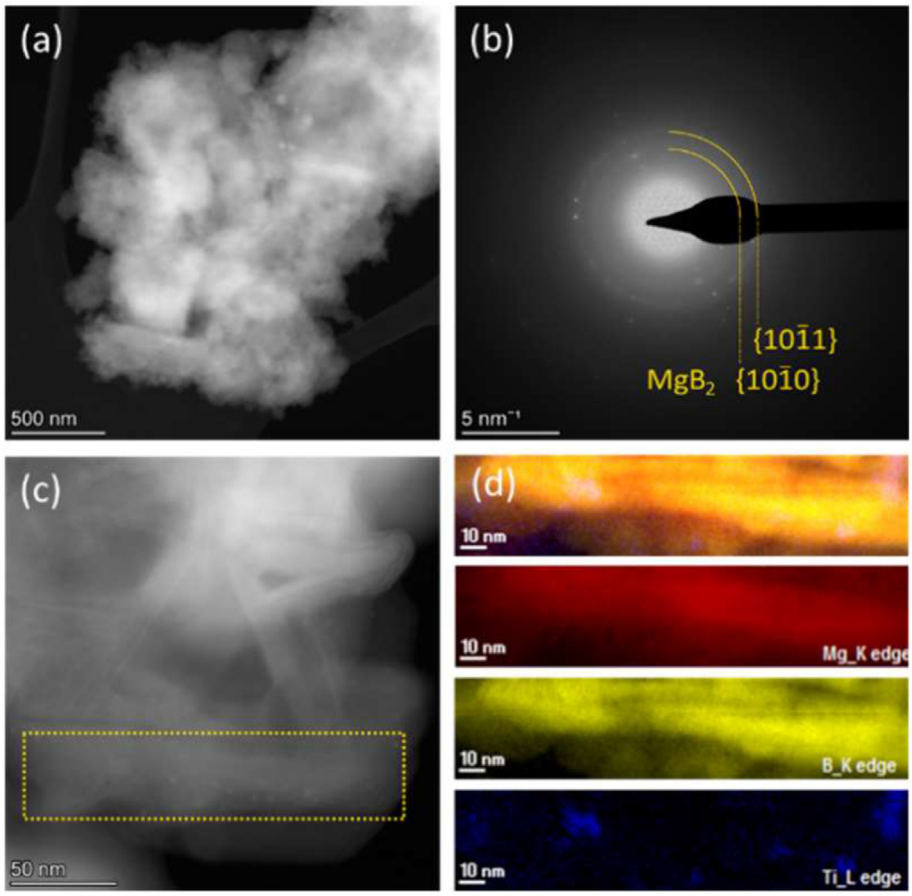

Fig. 4 – (a) TEM and (b) the corresponding FFT images of the Na-RHC + 5mol% $3TiCl_3 \cdot AlCl_3$ sample after dehydrogenation. (c) Enlarged image of the area shown in (a). (d) The corresponding EELS mapping of different elements, including Mg, B, and Ti for (c). The crystallographic information of the rings on the diffraction pattern comes from the entire region in (a).

EDX mappings of Ti and B indicate that both overlap. Hence, this result suggests that nanostructured TiB_2 is present and results from the reaction between the additives and the starting materials.

As can be seen in the HAADF image (Fig. 5(a)) and corresponding EDX mapping (Fig. 5(b)–(d)) of the formed MgB_2 for the sample doped with 5 mol% $3TiCl_3 \cdot AlCl_3$ after dehydrogenation, the needle like structure presented in Fig. 5(a) is proved to be MgB_2. To further investigate the effects of $3TiCl_3 \cdot AlCl_3$ additive on the formation of MgB_2, HRTEM was used to verify the size and shape of the represented MgB_2 in the sample doped with 5 mol% $3TiCl_3 \cdot AlCl_3$. Fig. 5(e), (f), and (g) show the areas that contain needle like MgB_2 particles with a thickness of 10–20 nm, in different magnifications. Fig. 5(h) is the corresponding fast Fourier transform (FFT) pattern of Fig. 5(g), which proves that the observed particles belong to the MgB_2 {0002} plane.

Fig. 6(a), (b), (c) and the fast Fourier transform (FFT) pattern (d) confirm the formation of TiB_2 and/or AlB_2 (abbreviated with "/") from the $3TiCl_3 \cdot AlCl_3$ additive as suggested by the equilibrium phase compositions calculation (Table 1). The detected spherical TiB_2/AlB_2 nanoparticles appear in a size range between 1 and 5 nm. The corresponding FFT pattern of Fig. 6(c) proves that the particle orientation correlates with the [211] zone axis of TiB_2/AlB_2, as shown in Fig. 6(d) and (e).

Size distribution of the boride additives

TEM investigation provided an insight into the morphology of the formed MgB_2 and the sizes of the compounds formed by the interaction of the additives with the Na RHC. In the following, it is investigated if these locally observed structures are evenly distributed in the samples. For this, SAXS analyses of the pure Na RHC and Na RHC + 5 mol% $3TiCl_3 \cdot AlCl_3$ after dehydrogenation were performed, and the results are reported in Fig. S12. Based on the results obtained by TEM, a cylindrical shaped particle geometry for fitting the SAXS data concerning the MgB_2 particles has been applied. As shown in the fitting result (Fig. 7(a)), the MgB_2 particles in the dehydrogenated pure Na RHC appear to have a mean diameter of 47 nm. In addition, the average length of these MgB_2 particles is 284 nm. Instead, for the dehydrogenated $3TiCl_3 \cdot AlCl_3$ doped sample, the average diameter and length of MgB_2 particles are reduced to 28.0 nm and 110 nm, respectively. Thus, the size of the MgB_2 particles in the sample with the $3TiCl_3 \cdot AlCl_3$ additive is 86% smaller than for the pure Na RHC. These SAXS measurements results show that the MgB_2 needle like structures observed by TEM are not a local singularity since they are homogeneously distributed all over the sample. However, due to the range of dimensions investigated (100 nm), a description of the morphology of the MgB_2 particles larger than 100 nm cannot be given. Based on the TEM investigation, the average dimension of the TiB_2/AlB_2 falls in the range of few nanometers, *i.e.*, 1–5 nm (Fig. 6). While observing the SAXS spectra, we can see that, for the dehydrogenated $3TiCl_3 \cdot AlCl_3$ doped sample, some structures are present in the range between 1 and 5 nm and are well described by a spherical symmetry model, as shown in Fig. 7(b). The mean radius of these structures is 1.5 nm. Besides, bigger particles have a mean diameter of 7.2 nm. Therefore, the TiB_2/AlB_2 nanoparticle structures observed in the TEM analyses are supported by SAXS outcomes.

Kinetic modeling

In order to understand the effects of additives on the dehydrogenation of $NaBH_4$ and nucleation of MgB_2, the rate limiting mechanism was evaluated using the Sharp and

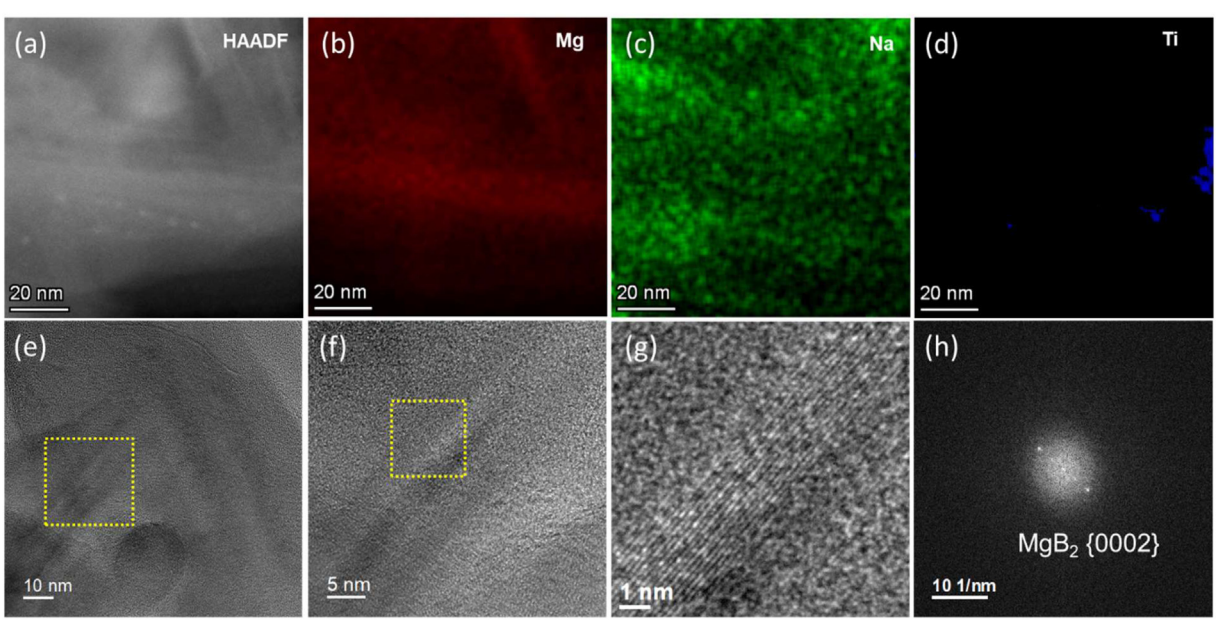

Fig. 5 – (a) HAADF image and (b)–(d) corresponding Mg, Na, and Ti EDX mapping of the formed MgB_2 for the sample doped with 5 mol% $3TiCl_3 \cdot AlCl_3$ after dehydrogenation. (e) HRTEM image of the formed MgB_2. (f) The enlarged image of the selected area shown in (a). (g) The enlarged image of the selected area in (b). (h) The corresponding FFT profile of (g).

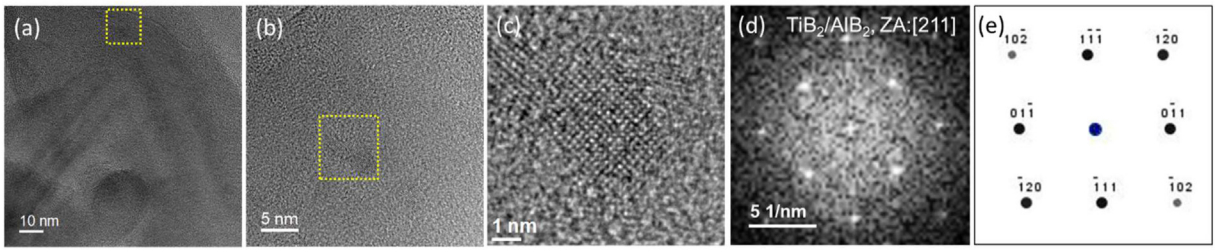

Fig. 6 – (a) HRTEM images of the sample doped with 5 mol% $3TiCl_3 \cdot AlCl_3$ after dehydrogenation. (b) The enlarged image of the selected area shown in (a). (c) The enlarged image of the selected area in (b). (d) The corresponding FFT profile of (c). (e) The simulated diffraction pattern of TiB_2/AlB_2.

Jones method [55,56]. The analyses were carried out for the second step of the dehydrogenation reactions since it covers about 80% of the hydrogen release and is slower. The reacted fractions considered for that are 0.1–0.7 (for pure Na RHC) and 0.1–0.8 (for Na RHC + 5 mol% $3TiCl_3 \cdot AlCl_3$) as shown in Fig. S13. Note that the reaction fraction of 0.1–0.7 and 0.1–0.8 is the fraction of the second dehydrogenation process, which means that the initial values of the overall reaction (the first plus the second dehydrogenation process) are 0.34–0.78 and 0.33–0.85, respectively. The results of the pristine sample and the one doped with $3TiCl_3 \cdot AlCl_3$ can be seen in Table 4, whereas the corresponding fitting parameters can be seen in Fig. S14 and Tables S13–14. For the pure Na RHC, the rate limiting step is two dimensional interface controlled (R2), indicating that the reaction is controlled by the interface movements toward the center of the crystal [64]. For the sample doped with 5 mol% $3TiCl_3 \cdot AlCl_3$, the rate limiting step changes to the F2 Johnson Mehl Avrami (JMA) model. The main limiting factor is random nucleation with one dimensional diffusion having a constant number of nuclei (F2) [65,66], The original and fitting curves by R2 and F2 models of these two samples are shown in Fig. 8. We suggest that the reaction kinetics depends markedly on the number and type of nucleation sites present in the system, defining the diffusion lengths. However, the proposed fittings are not fully satisfactory in particular for what concerns the pure Na RHC. Although to give an accurate description of the reasons for the observed divergences is not easy, a careful analysis of what is already known about this system might help. In his PhD dissertation, one of the coauthors of this manuscript [59] reported on the formation of a $NaH-NaBH_4$ molten phase during the dehydrogenation of the system $2NaBH_4+MgH_2$ for temperature higher than 380 °C. Thus, the second step of dehydrogenation of $2NaBH_4+MgH_2$ starts with an interaction between solid $NaBH_4$ and Mg to form NaH and MgB_2. However, as soon as NaH is available, it interacts with a portion of the still present $NaBH_4$ to form a $NaH-NaBH_4$ molten phase. At this point, the formation of the products Na/NaH + MgB_2 might follow multiple competing paths, *i.e.*, by the interaction of the $NaH-NaBH_4$ molten phase with Mg or by the interaction of the remaining solid $NaBH_4$ with Mg. Thus, the discrepancies between the experimental data and the kinetic fitting might arise from the fact that the reaction mechanisms at the base of the second dehydrogenation step of the system

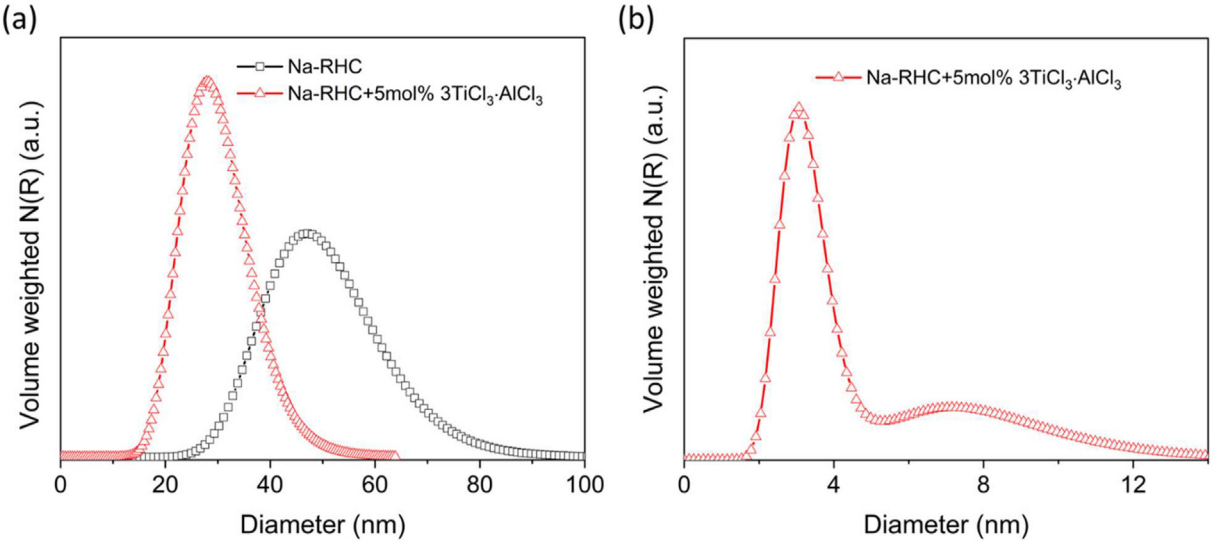

Fig. 7 – (a) Size distribution of MgB_2 particles in dehydrogenated pure Na-RHC and Na-RHC + 5 mol% $3TiCl_3 \cdot AlCl_3$ samples. (b) Size distribution of TiB_2/AlB_2 in dehydrogenated Na-RHC + 5 mol% $3TiCl_3 \cdot AlCl_3$ sample. Note the different scale for the diameters in (a) and (b).

Table 4 – Kinetic models for dehydrogenation of Na-RHC and Na-RHC + 5 mol% $3TiCl_3 \cdot AlCl_3$.		
Composition	Kinetic model	Rate limiting mechanism
Na RHC	R2	Two dimensional interface controlled
Na RHC + 5mol% $3TiCl_3 \cdot AlCl_3$	F2	Random nucleation with one dimensional diffusion having a constant number of nuclei

$2NaBH_4+MgH_2$ are multiple and occur simultaneously in a competitive manner.

Role of additives on the reaction kinetics and morphology

Compared to the pure Na RHC, adding 5 mol% of $3TiCl_3 \cdot AlCl_3$ (Fig. 2(a)) markedly improves the dehydrogenation kinetics of Na RHC + 5 mol% $3TiCl_3 \cdot AlCl_3$ and significantly modifies the MgB_2 particle morphology. The possible reasons lying behind such changes are discussed in the following.

Firstly, the smaller particle size of MgB_2 in the doped sample (Fig. 7(a)), 86% smaller than in the pure sample, leads to an increase in the surface area of MgB_2. Such an increase in surface area of MgB_2 is an essential factor during dehydrogenation because an increased number of nucleation sites of these smaller MgB_2 structures might lead to smaller diffusion distances for the B and Mg carrying species. Thus the change in morphology of MgB_2 can promote the reaction rate. The enhancement of the dehydrogenation rate of the $3TiCl_3 \cdot AlCl_3$ doped samples is related to a faster formation of MgB_2. In this regard, the formed TiB_2/AlB_2 nanoparticles might act as additional nucleation centers [45] for MgB_2. However, evaluating if the TiB_2/AlB_2 nanoparticles are suitable nucleation centers for MgB_2, parameters such as interatomic and planar mismatches should be considered. In fact, when interatomic and planar mismatches between the parental and the nucleating phase are low, the elastic strain energy in the newly forming phase is low, and the nucleation process is favored. The minimum interfacial energy between adjacent phases is usually achieved by matching the close packed or nearly close packed planes. Based on the edge to edge model [67], a good matching orientation relationship should fulfill the criteria that its interatomic mismatch and interplanar mismatches are less than 10% and 6%, respectively [44,67].

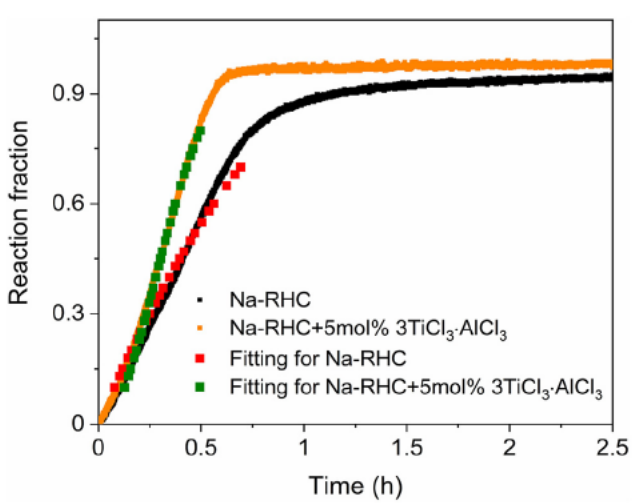

Fig. 8 – Reaction fraction versus time plots for the pure Na-RHC and Na-RHC + 5 mol% $3TiCl_3 \cdot AlCl_3$ samples, the fitting curves of R2 model for pure Na-RHC and F2 model for Na-RHC + 5 mol% $3TiCl_3 \cdot AlCl_3$ are also shown. (For interpretation of the references to color/colour in this figure legend, the reader is referred to the Web version of this article.)

Therefore, the interatomic and planar mismatches being important quantities to understand the role of the additives on the dehydrogenation behavior of Na RHC, these values were calculated for several phases related to the nucleation of MgB_2 in the pure and the $3TiCl_3 \cdot AlCl_3$ doped system. As reported in Table 5, the calculated interatomic mismatch between MgB_2 and TiB_2/AlB_2 (1.74% for <11–20>MgB_2 ‖ <11–20> TiB_2 and 2.53% for <11–20>MgB_2 ‖ <11–20> AlB_2) is smaller than that between MgB_2 and Mg (2.54% for <10 10>MgB_2 ‖ <0001>Mg. In addition, The interplanar mismatch between MgB_2 and TiB_2 (1.74% for {10 10}MgB_2 ‖ {10 10}TiB_2) is smaller than the mismatch between MgB_2 and Mg (2.55% for {10 10}MgB_2 ‖ {0001}Mg), and the mismatch between MgB_2 and AlB_2 is 2.67% (for {10 10}MgB_2 ‖ {10 10}AlB_2). Thus, the smaller interatomic and interplanar mismatches between MgB_2 and TiB_2/AlB_2 are expected to provide a kinetically favored path for the nucleation of MgB_2 in the $3TiCl_3 \cdot AlCl_3$ doped system compared to the pure system. Furthermore, the Na RHC + 5 mol% $3TiCl_3 \cdot AlCl_3$ material presents a refined MgB_2 microstructure and a homogenous distribution of needle like MgB_2 and spherical like transition metal borides (Sections 3.4 and 3.5). Hence, the suitable interatomic and interplanar mismatches between MgB_2 and TiB_2/AlB_2, the refined microstructure, and the homogenous distribution of nuclei sites enhance the interphase nucleation avoiding the interphase controlled mechanism. Thus, faster dehydrogenation kinetics can be observed in Fig. 2(a).

The TEM analyses reported in Figs. 3 and 4 showed that the MgB_2 in the pristine Na RHC has a plate like structure, whereas the $3TiCl_3 \cdot AlCl_3$ doped sample has a needle like structure. These results are well in agreement with the work of Lee et al. [68] and Jin et al. [45]. In fact, in their work, Lee et al. claimed that the growth of MgB_2 crystal takes place preferentially in two dimensions, while the growth on the third (i.e., c axis [0002]) is hindered, leading to MgB_2 morphologies similar to those observed in this work, *e.g.*, plate like and needle like. The produced MgB_2 in both samples may have a needle like shape. However, in the undoped sample, MgB_2 growth occurs on a parental phase (*i.e.*, Mg) with a diameter of several micrometers (Fig. 7(a)), which could result in side by side

Table 5 – Calculated interatomic and interplanar mismatch between MgB_2 and several possible phases.

Composition	Matching directions	Interatomic mismatch (%)	Matching planes	Interplanar mismatch (%)
TiB_2	<11 20>MgB_2 ‖ <11 20> TiB_2	1.74	{10 10}MgB_2 ‖ {10 10}TiB_2	1.74
AlB_2	<11 20>MgB_2 ‖ <11 20> AlB_2	2.53	{10 10}MgB_2 ‖ {10 10}AlB_2	2.67
Mg	<10 10>MgB_2 ‖ <0001>Mg	2.54	{10 10}MgB_2 ‖ {0001}Mg	2.55

clustering of many needles in a particular direction. On the contrary, in the doped samples, the parental phases (*e.g.*, TiB_2/AlB_2) have a particle dimension of few nanometers that does not allow for the formation of multiple needles and their clustering. Thus, the needles appear as single entities randomly oriented. However, to further understand the mechanisms of action of the additives at the atomic scale, additional theoretical calculations and computer based sim ulations will be carried out in the near future. Due to the wide range of possible reaction mechanisms that this system ex hibits depending on the applied temperature and pressure settings [69,70], the rehydrogenation process of the analyzed systems was not investigated in this work.

Conclusions

In this work, the effects of the TM based additives, *i.e.*, MgF_2, $3TiCl_3{\cdot}AlCl_3$, VCl_3, and $Mg(OH)_2$ on the dehydrogenation ki netics of the $2NaBH_4 + MgH_2$ system were investigated. The conclusions are as follows:

(1) The $3TiCl_3{\cdot}AlCl_3$ doped sample shows the fastest dehydrogenation kinetics, *e.g.*, 8.0 wt% of hydrogen can be released in 3 h.
(2) Equilibrium phase composition calculations show that TiB_2/AlB_2 particles can be formed after dehydrogena tion, verified by TEM analyses.
(3) The MgB_2 in the doped sample exhibits a needle like structure, as observed by 2D images, which differs from the plate like structure of the un doped sample.
(4) Rate limiting mechanism of the second step of the dehydrogenation reaction shows that the addition of $3AlCl_3{\cdot}AlCl_3$ changes the reaction mechanism from a two dimensional interface controlled reaction to random nucleation with one dimensional diffusion having a constant number of nuclei. Therefore, the *in situ* formed transition nanostructured metal borides and the refined needle like shape of MgB_2 accelerate the interface controlled mechanism of the MgB_2 nuclei formation upon dehydrogenation. The reasons why the combination of the *in situ* formed nanostructured metal borides and the refined needle like shape of MgB_2 improve the dehydrogenation kinetic behavior of Na RHC can be attributed to: First, the additives disperse the particles of $NaBH_4$ and MgH_2 more homogenously, which offers more nucleation sites for MgB_2. Second, a smaller misfit between MgB_2 and TiB_2/AlB_2 is expected to weaken the nucleation barrier, thus promoting the reaction rate.

Declaration of competing interest

The authors declare that they have no known competing financial interests or personal relationships that could have appeared to influence the work reported in this paper.

Acknowledgments

This work was supported by Deutsche For schungsgemeinschaft (DFG) [grant numbers PU 131/16 1 and PI 1488/2 1, No. 425395402]; dtec.bw Digitalization and Technology Research Center of Bundeswehr; Karlsruhe Nano Micro Facility (KNMF); National Research Council of Thailand (NRCT); and Suranaree University of Technology [grant num ber N42A650323].

Appendix A. Supplementary data

Supplementary data to this article can be found online at https://doi.org/10.1016/j.ijhydene.2022.08.293.

REFERENCES

[1] Dunn S. On hydrogen futures: toward a sustainable energy system author's reply. Int J Hydrogen Energy 2003;28:135 6.
[2] Winter CJ. Hydrogen energy abundant, efficient, clean: a debate over the energy system of change. Int J Hydrogen Energy 2009;34:S1 52.
[3] Momirlan M, Veziroglu TN. Current status of hydrogen energy. Renew Sustain Energy Rev 2002;6:141 79.
[4] Pistidda C. Solid State Hydrogen Storage for a Decarbonized Society. Hydrogen 2021;2:428 43.
[5] Tzimas E, Filiou C, Peteves S, Veyret JB. Hydrogen storage: state of the art and future perspective. 2003.
[6] Hoogers G. Fuel cell technology handbook. CRC press; 2002.
[7] Zecevic S, Patton EM, Parharni P. Carbon air fuel cell without a reforming process. Carbon 2004;42:1983 93.
[8] Hayes MD, Xin H, Li H, Shepherd TA, Stinn JP. Electricity and fuel use of aviary laying hen houses in the midwestern United States. Appl Eng Agric 2014;30:259 66.
[9] Jensen JO, Vestbo AP, Li Q, Bjerrum NJ. The energy efficiency of onboard hydrogen storage. J Alloys Compd 2007;446:723 8.
[10] Milanese C, Jensen TR, Hauback BC, Pistidda C, Dornheim M, Yang H, et al. Complex hydrides for energy storage. Int J Hydrogen Energy 2019;44:7860 74.
[11] Schneemann A, White JL, Kang S, Jeong S, Wan LWF, Cho ES, et al. Nanostructured metal hydrides for hydrogen storage. Chem Rev 2018;118:10775 839.

[12] Schlapbach L, Zuttel A. Hydrogen storage materials for mobile applications. Nature 2001;414:353 8.
[13] Dillon AC, Jones KM, Bekkedahl TA, Kiang CH, Bethune DS, Heben MJ. Storage of hydrogen in single walled carbon nanotubes. Nature 1997;386:377 9.
[14] Ley MB, Jepsen LH, Lee YS, Cho YW, von Colbe JMB, Dornheim M, et al. Complex hydrides for hydrogen storage new perspectives. Mater Today 2014;17:122 8.
[15] Dematteis EM, Berti N, Cuevas F, Latroche M, Baricco M. Substitutional effects in TiFe for hydrogen storage: a comprehensive review. Mater Adv 2021;2:2524 60.
[16] Wang H, Wu GT, Cao HJ, Pistidda C, Chaudhary AL, Garroni S, et al. Near ambient condition hydrogen storage in a synergized Tricomponent hydride system. Adv Energy Mater 2017;7.
[17] Abe JO, Popoola API, Ajenifuja E, Popoola OM. Hydrogen energy, economy and storage: review and recommendation. Int J Hydrogen Energy 2019;44:15072 86.
[18] Tarasov BP, Fursikov PV, Volodin AA, Bocharnikov MS, Shimkus YY, Kashin AM, et al. Metal hydride hydrogen storage and compression systems for energy storage technologies. Int J Hydrogen Energy 2021;46:13647 57.
[19] Kovac A, Paranos M, Marcius D. Hydrogen in energy transition: a review. Int J Hydrogen Energy 2021;46:10016 35.
[20] Mueller WM, Blackledge JP, Libowitz GG. Metal hydrides. Elsevier; 2013.
[21] Orimo SI, Nakamori Y, Eliseo JR, Zuttel A, Jensen CM. Complex hydrides for hydrogen storage. Chem Rev 2007;107:4111 32.
[22] Orimo S, Nakamori Y, Kitahara G, Miwa K, Ohba N, Towata S, et al. Dehydriding and rehydriding reactions of LiBH4. J Alloys Compd 2005;404:427 30.
[23] Yadav M, Xu Q. Liquid phase chemical hydrogen storage materials. Energy Environ Sci 2012;5:9698 725.
[24] Bogdanovic B, Schwickardi M. Ti doped alkali metal aluminium hydrides as potential novel reversible hydrogen storage materials. J Alloys Compd 1997;253:1 9.
[25] Hagemann H. Boron hydrogen compounds: hydrogen storage and Battery applications. Molecules 2021;26.
[26] Hagemann H. Estimation of thermodynamic properties of metal Hydroborates. ChemistrySelect 2019;4:8989 92.
[27] Barkhordarian G, Klassen T, Bormann R. Metal containing hydrogen storing material and its production. PCT International Application 2005. WO2005068073A8WIPO (PCT).
[28] Vajo J, Mertens FO, Skeith S, Balogh MP. Reversible hydrogen storage system using hydride mixture. PCT International Application 2005. WO2005097671A2WIPO (PCT).
[29] Ali NA, Sazelee NA, Ismail M. An overview of reactive hydride composite (RHC) for solid state hydrogen storage materials. Int J Hydrogen Energy 2021;46:31674 98.
[30] Garroni S, Pistidda C, Brunelli M, Vaughan GBM, Suriñach S, Baró MD. Hydrogen desorption mechanism of 2NaBH4 + MgH2 composite prepared by high energy ball milling. Scripta Mater 2009;60:1129 32.
[31] Pottmaier D, Pistidda C, Groppo E, Bordiga S, Spoto G, Dornheim M, et al. Dehydrogenation reactions of 2NaBH4 + MgH2 system. Int J Hydrogen Energy 2011;36:7891 6.
[32] Milanese C, Garroni S, Girella A, Mulas G, Berbenni V, Bruni G, et al. Thermodynamic and kinetic investigations on pure and doped NaBH4 MgH2 system. J Phys Chem C 2011;115:3151 62.
[33] Stasinevich D, Egorenko G & Gnedina G. in Dokl. Akad. Nauk SSSR. 610 612.
[34] Garroni S, Milanese C, Pottmaier D, Mulas G, Nolis P, Girella A, et al. Experimental Evidence of Na 2[B12H12] and Na formation in the desorption Pathway of the 2NaBH(4) + MgH2 system. J Phys Chem C 2011;115:16664 71.
[35] Urgnani J, Torres FJ, Palumbo M, Baricco M. Hydrogen release from solid state NaBH4. Int J Hydrogen Energy 2008;33:3111 5.
[36] Linstorm P. NIST chemistry webbook, NIST standard reference database number 69. J Phys Chem Ref Data, Monograph 1998;9:1 1951.
[37] Deprez E, Justo A, Rojas TC, López Cartés C, Bonatto Minella C, Bösenberg U, et al. Microstructural study of the LiBH4 MgH2 reactive hydride composite with and without Ti isopropoxide additive. Acta Mater 2010;58:5683 94.
[38] Bonatto Minella C, Garroni S, Pistidda C, Baró MD, Gutfleisch O, Klassen T, et al. Sorption properties and reversibility of Ti(IV) and Nb(V) fluoride doped Ca(BH4)2 MgH2 system. J Alloys Compd 2015;622:989 94.
[39] Jiang Y, Liu B. Dehydrogenation kinetics of 2LiBH(4) + MgH2 enhanced by hydrogen back pressure and a CuCl2 catalyst. J Alloys Compd 2011;509:9055 9.
[40] Yuan PP, Liu BH, Li ZP. A comparative study of LiBH4 based composites with metal hydrides and fluorides for hydrogen storage. Int J Hydrogen Energy 2011;36:15266 72.
[41] Zhai B, Xiao XZ, Lin WP, Huang X, Fan XL, Li SQ, et al. Enhanced hydrogen desorption properties of LiBH4 Ca(BH4)(2) by a synergetic effect of nanoconfinement and catalysis. Int J Hydrogen Energy 2016;41:17462 70.
[42] Bosenberg U, Kim JW, Gosslar D, Eigen N, Jensen TR, von Colbe JMB, et al. Role of additives in LiBH4 MgH2 reactive hydride composites for sorption kinetics. Acta Mater 2010;58:3381 9.
[43] Karimi F, Pranzas PK, Pistidda C, Puszkiel JA, Milanese C, Vainio U, et al. Structural and kinetic investigation of the hydride composite Ca(BH4)(2) + MgH2 system doped with NbF5 for solid state hydrogen storage. Phys Chem Chem Phys 2015;17:27328 42.
[44] Zhang MX, Kelly PM, Easton MA, Taylor JA. Crystallographic study of grain refinement in aluminum alloys using the edge to edge matching model. Acta Mater 2005;53:1427 38.
[45] Jin O, Shang Y, Huang X, Mu X, Szabó DV, Le TT, et al. Microstructural study of MgB2 in the LiBH4 MgH2 composite by using TEM. Nanomaterials 2022;12:1893.
[46] Brinks HW, Fossdal A, Hauback BC. Adjustment of the stability of complex hydrides by anion substitution. J Phys Chem C 2008;112:5658 61.
[47] Czujko T, Varin RA, Wronski Z, Zaranski Z, Durejko T. Synthesis and hydrogen desorption properties of nanocomposite magnesium hydride with sodium borohydride (MgH2 + NaBH4). J Alloys Compd 2007;427:291 9.
[48] Barkhordarian G, Klassen T, Dornheim M, Bormann R. Unexpected kinetic effect of MgB2 in reactive hydride composites containing complex borohydrides. J Alloys Compd 2007;440:L18 21.
[49] Ares Fernandez JR, Aguey Zinsou KF. Superior MgH2 kinetics with MgO addition: a Tribological effect. Catalysts 2012;2:330 43.
[50] Cullity BD. Elements of X ray diffraction. Am J Phys 1957;25:394 5.
[51] Roine A. HSC Chemistry for windows chemical reaction and equilibrium software with extensive thermochemical database. *Outokumpu, HSC chemistry for windows chemical ReOutokumpu research oy. Pori.* 1999.
[52] Bouamrane A, de Brauer C, Soulie JP, Letoffe JM, Bastide JP. Standard enthalpies of formation of sodium magnesium hydride and hydridofluorides NaMgH3, NaMgH2F and NaMgF2H. Thermochim Acta 1999;326:37 41.
[53] Bouhadda Y, Fenineche N, Boudouma Y. Hydrogen storage: lattice dynamics of orthorhombic NaMgH3. Physica B 2011;406:1000 3.

[54] Pottmaier D, Pinatel ER, Vitillo JG, Garroni S, Orlova M, Baro MD, et al. Structure and thermodynamic properties of the NaMgH3 Perovskite: a comprehensive study. Chem Mater 2011;23:2317 26.
[55] Sharp JH, Brindley GW, Achar BNN. Numerical data for some commonly used solid state reaction Equations. J Am Ceram Soc 1966;49:379 &.
[56] Jones LF, Dollimore D, Nicklin T. Comparison of experimental kinetic decomposition data with master data using a linear plot method. Thermochim Acta 1975;13:240 5.
[57] Mao JF, Gu QF, Guo ZP, Liu HK. Sodium borohydride hydrazinates: synthesis, crystal structures, and thermal decomposition behavior. J Mater Chem 2015;3:11269 76.
[58] Ouyang LZ, Chen W, Liu JW, Felderhoff M, Wang H, Zhu M. Enhancing the Regeneration process of Consumed NaBH4 for hydrogen storage. Adv Energy Mater 2017;7.
[59] Pistidda C. Hydrogen sorption properties of the composite system 2NaBH4+ MgH2. Technische Universität Hamburg; 2011.
[60] Fan MQ, Sun LX, Zhang Y, Xu F, Zhang J, Chu HL. The catalytic effect of additive Nb2O5 on the reversible hydrogen storage performances of LiBH4 MgH2 composite. Int J Hydrogen Energy 2008;33:74 80.
[61] Deprez E, Justo A, Rojas TC, Lopez Cartes C, Minella CB, Bosenberg U, et al. Microstructural study of the LiBH4 MgH2 reactive hydride composite with and without Ti isopropoxide additive. Acta Mater 2010;58:5683 94.
[62] Wang PJ, Ma LP, Fang ZZ, Kang XD, Wang P. Improved hydrogen storage property of Li Mg B H system by milling with titanium trifluoride. Energy Environ Sci 2009;2:120 3.
[63] Rude LH, Nielsen TK, Ravnsbaek DB, Bosenberg U, Ley MB, Richter B, et al. Tailoring properties of borohydrides for hydrogen storage: a review. Phys Status Solidi 2011;208:1754 73.
[64] Khawam A, Flanagan DR. Solid state kinetic models: Basics and mathematical fundamentals. J Phys Chem B 2006;110:17315 28.
[65] Puszkiel JA. In: Gold nanoparticles reaching new heights. London, UK: IntechOpen; 2018.
[66] Christian JW. The theory of transformations in metals and alloys. Newnes; 2002.
[67] Kelly PM, Zhang MX. Edge to edge matching the fundamentals. Metall Mater Trans A 2006;37a:833 9.
[68] Lee S. Crystal growth of MgB2. Physica C 2003;385:31 41.
[69] Garroni S, Milanese C, Girella A, Marini A, Mulas G, Menéndez E, et al. Sorption properties of NaBH4/MH2 (M = Mg, Ti) powder systems. Int J Hydrogen Energy 2010;35:5434 41.
[70] Mao JF, Yu XB, Guo ZP, Liu HK, Wu Z, Ni J. Enhanced hydrogen storage performances of NaBH4 MgH2 system. J Alloys Compd 2009;479:619 23.